Preprint of manuscript published in Faraday Discussions, Vol. 194, 731-746, 2016

Journal Name

ARTICLE TYPE

Cite this: DOI: 10.1039/xxxxxxxxxx

# Probing Spin-Vibronic Dynamics Using Femtosecond X-ray Spectroscopy†

T.J. Penfold,*[a] M. Pápai,[b,c], T. Rozgonyi[d], K.B. Møller [b] and G. Vankó [c]

Received Date
Accepted Date

DOI: 10.1039/xxxxxxxxxx

www.rsc.org/journalname

Ultrafast pump-probe spectroscopy within the X-ray regime is now possible owing to the development of X-ray Free Electrons Lasers (X-FELs) and is opening new opportunities for the direct probing of femtosecond evolution of the nuclei, the electronic and spin degrees of freedom. In this contribution we use wavepacket dynamics of the photoexcited decay of a new Fe(II) complex, $[Fe(bmip)_2]^{2+}$(bmip=2,6-bis(3-methyl-imidazole-1-ylidine)pyridine), to simulate the experimental observables associated with femtosecond Fe K-edge X-ray Absorption Near-Edge Structure (XANES) and X-ray Emission (XES) spectroscopy. We show how the evolution of the nuclear wavepacket is translated into the spectroscopic signal and the sensitivity of these approaches for following excited state dynamics.

## 1 Introduction

To observe, understand and exploit the simultaneous evolution of nuclear, electronic and spin degrees of freedom on the atomic scale of time, i.e. femtoseconds, is a great challenge with far reaching implications. This is especially pertinent for our understanding of processes occurring within electronically excited states. Metal organic complexes are excellent model systems to study the correlation between these fundamental degrees of freedom[1], but are also of significant interest in their own right due to often remarkable photophysical behaviour and versatility[2,3]. Indeed after photoexitation, these molecular complexes may undergo any of a plethora of important phenomena including radiative (fluorescence and phosphorescence) decay, non-radiative intramolecular relaxation processes, such as internal conversion (IC) intersystem crossings (ISC, i.e. a spin change) and intramolecular vibrational redistribution (IVR). Most of these processes are accompanied or driven by structural changes occurring as the nuclei adapt to the new electronic structure. Consequently, the relative fraction of these pathways can often be manipulated by modifying the chemical composition[4] or by an external perturbation[5].

Besides the study of fundamental photophysical processes, transition metal complexes have also gathered significant attention owing to potential applications, such as photosensitisers in photovoltaics or photocatalysts[6,7]. At the heart of such applications are the photoactive metal-to-ligand charge transfer (MLCT) states. The importance of these states has meant that Fe(II) complexes are generally considered inappropriate as their MLCT states are typically very short lived[8,9] owing to the presence of low-lying metal centered (MC) states[10]. However, Liu *et al.*[11] recently demonstrated that by exploiting the strong field effects of NHC ligands to create $[Fe(bmip)_2]^{2+}$(bmip=2,6-bis(3-methyl-imidazole-1-ylidine)pyridine), as shown in Figure 1a, it was possible to destabilise the MC states and significantly increase MLCT lifetime. Using ultrafast transient absorption they reported a $^1$MLCT$\rightarrow^3$MLCT conversion of $\sim$100 fs, no population of a high spin $^5T_2$ state and a $^3$MLCT lifetime of $\sim$9 ps[11].

Our understanding of these ultrafast processes within metal organic complexes has increased enormously with the emergence of femtosecond pump-probe spectroscopies, and the rapid development within this area has made it possible to tackle increasingly complicated dynamical processes. This complexity provides a strong driving force for combining complementary spectroscopic techniques to resolve a full understanding of excited state dynamics. However, until recently this spectroscopic toolkit has not included techniques within the short wavelength regime[12]. In particular ultrafast X-ray experiments, made possible by the advent of X-ray Free Electron Lasers[13,14] and which are beginning to provide complementary information about a wide range of interesting systems[8,15–18].

Advancements in experimental techniques also call for development of theoretical methodologies. In terms of ultrafast X-

[a] *School of Chemistry, Newcastle University, Newcastle upon Tyne, NE1 7RU, United Kingdom. tom.penfold@ncl.ac.uk*
[b] *Department of Chemistry, Technical University of Denmark, DK-2800, Kongens Lyngby, Denmark.*
[c] *Wigner Research Centre for Physics, Hungarian Academy of Sciences, P.O. Box 49, H-1525 Budapest, Hungary.*
[d] *Institute of Materials and Environmental Chemistry, Research Centre for Natural Sciences, Hungarian Academy of Sciences, P.O. Box 286, H-1519 Budapest, Hungary.*
† Electronic Supplementary Information (ESI) available: [details of any supplementary information available should be included here]. See DOI: 10.1039/b000000x/

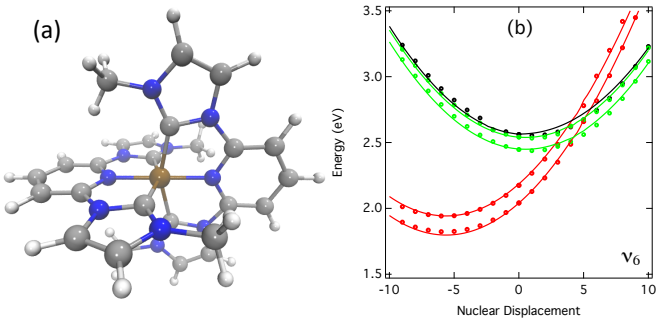


**Fig. 1** (a) Molecular structure of $[Fe(bmip)_2]^{2+}$. (b) Cut through the spin-free potential energy curves along $\nu_6$, the most important for the excited state dynamics of $[Fe(bmip)_2]^{2+}$. The dots are derived from the quantum chemistry calculations. The lines correspond to their fit from which the expansion coefficients of the diabatic Vibronic Coupling Hamiltonian are determined. Colour code is as follows: $^1$MLCT: black, $^3$MLCT: green and $^3$MC: red.

ray spectroscopy, this means going beyond simulations of metastable states[19] and requires accurately including excited states dynamics with nonadiabatic effects. Recently, Capano *et al.* applied quantum dynamics simulations of a prototypical Cu(I)-phenanthroline complex, $[Cu(dmp)_2]^+$ (dmp = 2, 9-dimethyl-1,10-phenanthroline)[20,21] to simulate femtosecond X-ray spectroscopic signals[22]. Using realistic experimental parameters they also derived the anticipated signal strengths. This showed that it would be possible to resolve the fine spectral details associated with wavepacket dynamics within realistic experimental acquisition times. Indeed, this was recently confirmed experimentally by Lemke *et al.*[23] for $[Fe(bipy)_3]^{2+}$. In addition, the time-resolved Extended X-ray Absorption Fine Structure (EXAFS) signals were shown to be very effective for probing the width as well as the position of the wavepacket and therefore will provide strong insight into the dynamics associated with vibrational cooling. In this contribution we extend our recent quantum dynamics simulations of $[Fe(bmip)_2]^{2+}$[24] to predict femtosecond X-ray spectroscopy, and in particular the experimental observables associated with X-ray Absorption Near Edge Spectroscopy (XANES) and X-ray Emission (XES). This combination provides insight into structural, electronic and spin dynamics of the $^{1,3}$MLCT and $^3$MC states. The implications of these simulations on future studies of molecular photophysics at X-FELs is also discussed.

## 2 Methods and Computations

### 2.1 Vibronic Coupling Hamiltonian

The potential used in the present work is based upon the Vibronic Coupling Hamiltonian model[25] and has been described in detail in ref.[24]. Briefly, the diabatic basis is fixed by choosing a point at which it is equal to the adiabatic basis (i.e. the coupling is zero), in this case the Franck-Condon point. The Hamiltonian is expanded as a Taylor series around this point $\mathbf{Q}_0$, using dimensionless (mass-frequency scaled) normal mode coordinates:

$$\mathbf{H} = \mathbf{H}^{(0)} + \mathbf{W}^{(0)} + \mathbf{W}^{(1)} + \ldots \quad (1)$$

The zeroth order term ($\mathbf{H}^{(0)}$) is the ground state harmonic oscillator approximation. The zeroth order coupling matrix ($\mathbf{W}^{(0)}$) contains the adiabatic state energies at $\mathbf{Q}_0$. The first order linear coupling matrix elements are written:

$$W_{ij}^{(1)} = \sum_\alpha \langle \Phi_i(\mathbf{Q}_0) | \frac{\partial H_{el}}{\partial Q_\alpha} | \Phi_j(\mathbf{Q}_0) \rangle Q_\alpha \quad (2)$$

Here, the on-diagonal elements are the forces acting within an electronic surface and the off-diagonal elements are the nonadiabatic couplings. The expansion coefficients for these terms, and those at higher order are obtained from a fit to the potential energy curves along the most important normal modes ($\alpha$). Similar approaches have recently been used in the case of Cu(I)[20,21] and Re(I)[26] transition metal complexes.

In ref.[24] we used symmetry rules of the $D_{2d}$ point group to simplify the determination of nonadiabatic coupling elements. We identified four normal modes, which are most important for describing the excited state dynamics. These are a totally symmetric breathing mode ($\nu_6$), two antisymmetric stretching modes ($\nu_{11}$ and $\nu_{25}$), predominately acting on the Fe-C bonds with symmetry $b_2$, and another totally symmetric breathing ($\nu_{36}$) mode with symmetry $a_1$, predominantly acting on the Fe-N bonds. $\nu_6$, whose potential energy curves are shown in Figure 1b, is the dominant vibrational mode of $[Fe(bmip)_2]^{2+}$and is used during the calculations of the excited state core-hole spectra.

Although a model including only four nuclear degrees of freedom clearly represents a significant reduction in the dimensionality of the potential, this is consistent with the excited state dynamics of many Fe(II) complexes, whose dynamics are usually well represented schematically using one vibrational coordination. Consequently, although the present Hamiltonian is unable to capture longer time effects, such as vibrational cooling, this component has little influence on the ultrafast dynamics.

The potential energy surfaces of the singlet and triplet states were calculated and fitted separately yielding two sets of spin-free potential energy surfaces. The coupling of the two manifolds to create the spin-vibronic potential energy surfaces was treated as a perturbation to the spin-free potential energy curves and was achieved by including the spin-orbit coupling matrix elements between all of the states considered. The potential energy surfaces were calculated using TDDFT(B3LYP*)[27–30] within the Tamm-Dancoff approximation (TDA)[31] and a TZVP basis set as implemented within the ORCA quantum chemistry package[32]. The SOC matrix elements were computed at the ground state equilibrium geometry using the perturbative approach developed by Wang and Ziegler[33] as implemented within ADF[34–36]. A TZP basis set was used for all atoms and scalar relativistic effects were included using the ZORA[37,38] approximation. All the parameters for the potentials, nonadiabatic and spin-orbit couplings for the model used below are available in ref.[24] .

### 2.2 Quantum Dynamics

The excited state wavepacket simulations were performed using the Heidelberg Multi Configuration Time Dependent Hartree (MCTDH) package[39,40]. In this approach the wavefunction

*ansatz* is written as a linear combination of Hartree products:

$$\Psi(Q_1,...,Q_f,t) = \sum_{j_1=1}^{n_1} ... \sum_{j_f=1}^{n_f} A_{j_1...j_f}(t) \prod_{k=1}^{f} \varphi_{j_k}^{(k)}(Q_k,t) \qquad (3)$$

where $Q_1$,...,$Q_f$ are the nuclear coordinates, $A_{j_1...j_f}(t)$ are the time-dependent expansion coefficients and $\varphi_{j_k}^{(k)}$ are the time dependent basis functions for each $k$ (degree of freedom), known as single particle functions (SPFs). The SPFs used in MCTDH have two advantages: (1) fewer are required as they are variationally determined (2) the functions can be multi-dimensional particles containing more than one degree of freedom thus reducing the effective number of degrees of freedom.

The computational details for the quantum dynamics simulations are shown in Table 1. These ensured convergence of the dynamics for 4 ps. To initiate the excited state dynamics, the wavefunction in the ground state built using one-dimensional harmonic oscillator functions with zero initial momentum was impulsively excited into the lowest $^1$MLCT state at the Franck-Condon geometry.

**Table 1** Computational details for the MCTDH simulations of the 26 state spin-vibronic Hamiltonian. $N_i$ is the number of primitive harmonic oscillator discrete variable representation (DVR) basis functions used to describe each mode. $n_i$ are the number of single-particle functions used to describe the wavepacket on each state. Note that each triplet state has three components ($m_s = -1, 0, 1$) which are treated with the same number of basis functions.

| Modes | $N_i$ | $n_{S_0}$,$n_{S_1}$,$n_{S_2}$,$n_{S_3}$,$n_{S_4}$,$n_{T_1}$,$n_{T_2}$,$n_{T_3}$,$n_{T_4}$,$n_{T_5}$,$n_{T_6}$,$n_{T_7}$ |
|---|---|---|
| $\nu_6$ | 191 | 1,12,12,5,5,25,26,24,24,17,17,17 |
| $\nu_{11}$ | 61 | 1,12,12,5,5,25,26,24,24,17,17,17 |
| $\nu_{25}$ | 61 | 1,12,12,5,5,25,26,24,24,17,17,17 |
| $\nu_{36}$ | 61 | 1,12,12,5,5,25,26,24,24,17,17,17 |

### 2.3 Simulating the X-ray Spectra

The X-ray spectra of the non-stationary wavepacket was computed using a weighted sum of the spectra calculated at each grid point used in the simulations. The weighting corresponds to the magnitude of the nuclear wavepacket at that grid point. As the nuclear motion in the dynamics is dominated by the motion along $\nu_6$, all of the spectroscopic observables were calculated by projecting the wavepacket along this mode. For each spectra, a sum over all of the electronic states was performed, thus achieving a description of the full nuclear wavepacket.

The XANES simulations were performed using the finite difference method as implemented within the FDMNES package[41,42]. This uses a free form potential of radius 7.0 Å around the absorbing atom and includes scalar relativistic effects. Broadening due to the finite mean-free path of the photoelectron and the core-hole lifetime were accounted for using an arctangent convolution[43]. The XES spectra were computed within the one-electron approach[44,45] as implemented in the ORCA quantum chemistry package[32]. Computations used the B3LYP* functional[27–30] and the TZVP basis set[46,47]. All calculations included spin-orbit coupling (SOC), for which the SOC operator was approximated by the spin-orbit mean field method (SOMF)[48]. A Lorentzian lifetime broadening with full-width at half maximum (FWHM) of 2.5 eV was applied after the calculation to account for the initial and final state broadening.

For both the XANES and XES spectra the excited $^{1,3}$MLCT states were simulated by increasing the overall charge on the complex, i.e. using $[Fe(bmip)_2]^{3+}$. This, as discussed in more detail below, reflects the sensitivity of X-ray spectra to the local electronic structure of the iron, rather than the electronic structure of the whole complex. Finally, the relative energies of the calculated transitions are generally well reproduced compared to experiment. However, it is well documented that the absolute transition energies are usually in poor agreement with experiment[49]. This failure stems from the approximate exchange description within the exchange-correlation functionals and is associated with the self interaction error (SIE)[50]. This is usually corrected by applying a constant shift to the spectrum *a posteriori*[51,52]. In this case, as the spectra presented herein are not directly compared to experimental data, these shifts have not been included.

## 3 Results

### 3.1 Photoexcited decay of $[Fe(bmip)_2]^{2+}$

Figure 2a shows the population kinetics of the $^{1,3}$MLCT and $^3$MC states following excitation into the lowest $^1$MLCT states as obtained using the vibronic Hamiltonian outlined above and detailed in ref.[24]. The dynamics are dominated by two main processes. The first is an ultrafast ISC from $^1$MLCT$\rightarrow^3$MLCT, which has a time constant of $\sim$100 fs[24] in excellent agreement with previous experimental observations[11]. The rapid nature of this step is a result of the close energetic proximity of the $^1$MLCT and $^3$MLCT states, which promotes strong mixing and leads to efficient population transfer. Figure 2b shows the population kinetics for which the two MLCT states have been summed together. As mentioned above and discussed in below this is important in the context of the sensitivity of the X-ray spectroscopic approaches used herein.

The dominant dynamics in the context of the present work corresponds to the decay of the $^3$MLCT into the $^3$MC states. Our simulations show two components, a faster one, which dominants the timescale of the present study, especially at early times ($<$2 ps) and which has a time constant of $\sim$1 ps. This is followed by a slower component consistent with a time constant $\geq$4 ps consistent with ref.[11]. This population transfer ($^3$MLCT$\rightarrow^3$MC) step is between two triplet states and therefore can occur through two mechanisms, nonadiabatic or spin-orbit coupling. During the first 1-2 ps, both mechanisms contribute and this gives rise to the initial faster component of the decay dynamics. However at later times the contribution of nonadiabatic coupling is reduced due to a redistribution of population within the $^3$MLCT manifold, and this gives rise to the lower population kinetics[24]. This population transfer is slower than the $^1$MLCT$\rightarrow^3$MLCT transition because the population transfer predominantly occurs away from the crossing point between the $^3$MLCT-$^3$MC states, at or near the energy minimum geometry of the $^3$MLCT states. Crucially, the energetic separation of the $^3$MLCT-$^3$MC states is $>$0.1 eV and therefore re-

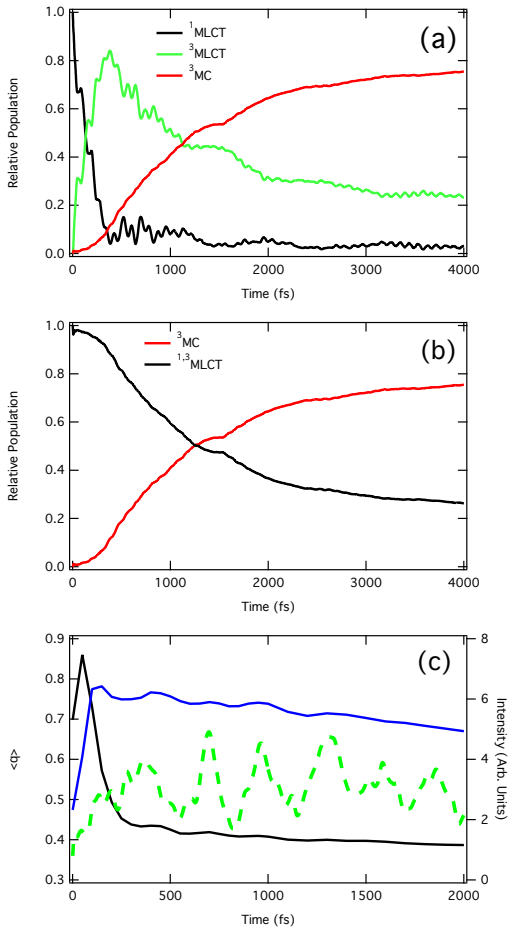


**Fig. 2** (a) Relative diabatic state populations of the $^1$MLCT (black), $^3$MLCT (green) and $^3$MC (red) states for 4 ps following photoexcitation. (a) Relative diabatic state populations of the $^{1,3}$MLCT (black) and $^3$MC (red) states for 4 ps following photoexcitation. (b) Expectation value of the position, <q> of the wavepacket in the $^3$MLCT state along $\nu_6$ (green) plotted with the transient absorption data in ref.[11] integrated between 600-680 nm (black) 510-538 nm (blue) corresponding to the $^1$MLCT and $^3$MLCT states, respectively.

gardless of the coupling strength, efficient population transfer is difficult.

Finally, previous experimental data[11] exhibits a weak oscillatory period close to 300 fs. This oscillatory component is very clearly observed in the wavepacket along $\nu_6$ (Figure 2c). These oscillations are stronger than observed experimentally due to the absence of the redistribution of vibrational energy within our model Hamiltonian. However, this does reveal that the principal nuclear dynamics during the excited state decay are dominated by the nuclear motion along one nuclear degree of freedom, in this present case $\nu_6$ with a period of 300 fs.

### 3.2 Femtosecond X-ray Spectroscopy

In this section we translate our quantum dynamics simulations[24] into ultrafast X-ray spectroscopic signals. As previously mentioned the X-ray techniques addressed herein are unable to distinguish between the $^{1,3}$MLCT states. XANES spectra are sensitive to the formal oxidation state and local geometry around the absorbing atom. Therefore the $^{1,3}$MLCT states are differentiated from the ground state and $^3$MC states due to a shift in the edge position to higher energies arising from the increased formal charge of the Fe following transfer of an electron from the metal to the ligands. As this formal charge of Fe is the same for both the $^{1,3}$MLCT states, they are indistinguishable. In contrast, the formal oxidation state of the latter ($^3$MC) remains the same as the ground state, however its edge position will shift to lower energies owing to the structural change of the state, i.e. bond elongations, as the position of the absorption edge depends inversely on the bond lengths of the atoms that coordinate to the absorbing atom[53].

In terms of the XES, sensitivity of the spectrum to spin state derives from the the K$\alpha$(2p→1s) and K$\beta$(3p→1s) emission through the 2p-3d and 3p-3d exchange integrals of the absorbing atom, respectively[54]. Given the short range nature of this interaction, the emission can be expected to be insensitive to the electronic properties of the ligand, both the $^{1,3}$MLCT will be characterised by the doublet spin state of the Fe, instead of the overall spin state of the complex.

#### 3.2.1 X-ray absorption near-edge structure (XANES)

Figure 3a shows the ground state XANES spectrum of $[Fe(bmip)_2]^{2+}$. It is characterised by a number of spectral features common to Fe K-edges of similar complexes and whose assignments were discussed in ref.[55]. The red traces show the difference (i.e. excited - ground state) spectra calculated for the MLCT states at the Franck-Condon geometry and the $^3$MC state at its optimised geometry. The former (dashed line) bears a strong resemblance to the difference spectrum of the MLCT states of $[Cu(dmp)_2]^+$[56]. In this case the spectrum is dominated by the edge shift and can, to a large extent, be reproduced using a *shifted difference* spectrum, i.e. energy-shifted ground-state spectrum minus the original ground-state spectrum. A similar situation is expected here, as the structure of the ground and $^{1,3}$MLCT states of $[Fe(bmip)_2]^{2+}$are very similar and therefore the main change is expected to be an edge shift associated with the change of oxidation state of the Fe. The transient spectrum of the $^3$MC states is characterised by a shift of the absorption edge to lower energy, owing to the expansion of the first coordination sphere. This spectrum exhibits, as expected, a similar profile to the transient spectrum of the metal centred states of $[Fe(bipy)_3]^{2+}$reported in ref.[57].

Figure 3b shows the temporal evolution of the transient XANES spectra during the first 2 ps after photoexcitation. At early times the spectrum, as expected from the population kinetics in Figure 2a, closely resembles the transient $^{1,3}$MLCT spectrum in Figure 3a. As the dynamics progresses the spectrum begins to exhibit increasing characteristics of the $^3$MC spectrum. There are also clear 300 fs oscillations in the transient signal, consistent with those observed in the transient absorption study[11,24]. As assigned above, this corresponds to the wavepacket motion along the $\nu_6$ breathing mode[24] and consequently it is similar to the widely reported wavepacket dynamics of $[Fe(bipy)_3]^{2+}$[9].

Figure 4 shows kinetic traces integrated over four main regions, namely 7119-7121 eV, 7122-7124 eV, 7131-7135 eV and 7136-

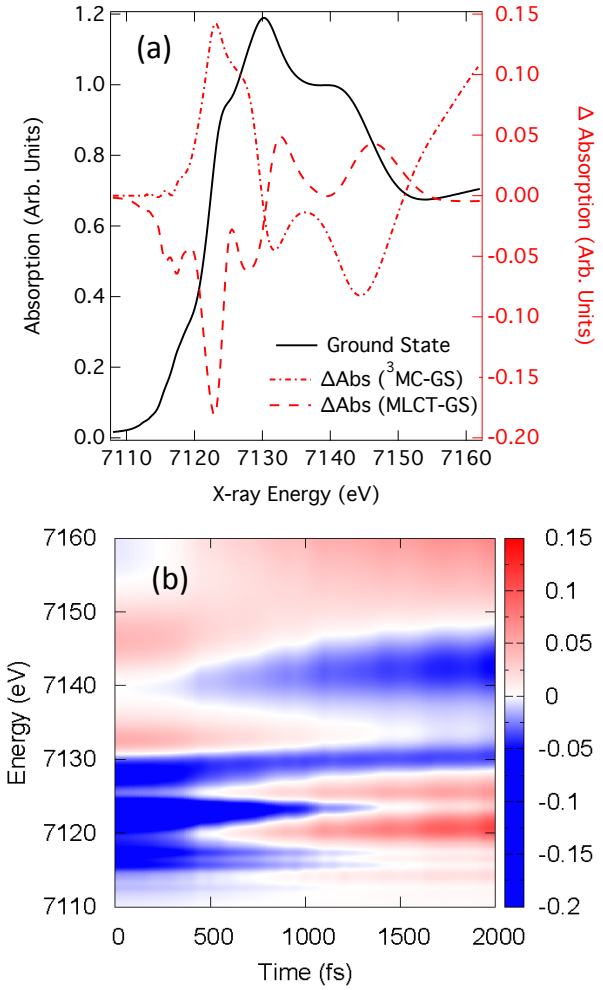


**Fig. 3** (a) The simulated ground state Fe K-edge XANES spectra and transient spectra corresponding to $^{1,3}$MLCT-GS (dashed line) and $^3$MC-GS (dotted and dashed line). (b) The transient XANES spectrum as a function of time, during 2 ps after photoexcitation.

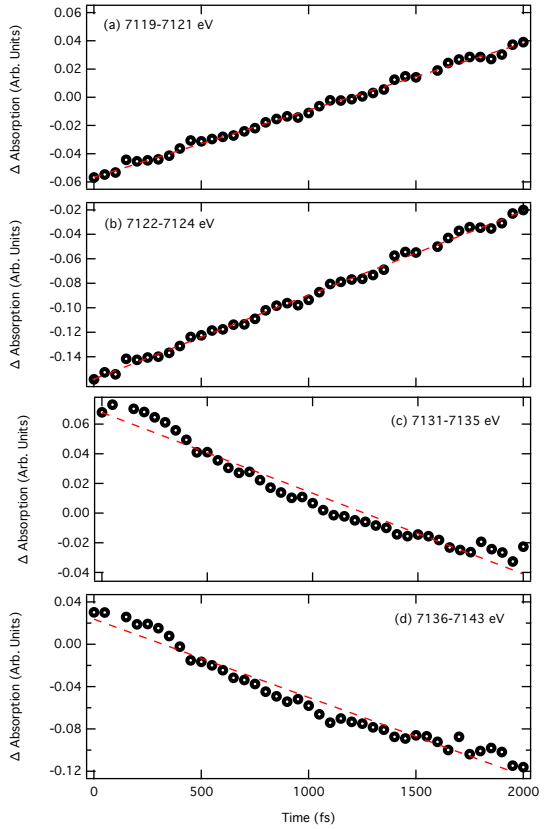


**Fig. 4** Time traces of the transient spectrum integrated between 7119-7121 eV (a), 7122-7124 eV (b), 7131-7135 eV (c) and 7136-7143 eV (d). The red dashed line corresponds to a linear fit of the kinetic traces.

7143 eV. The lowest two, which probe the pre- and rising edge of the Fe K-edge spectrum show a monotonic rise largely associated with the population transfer between the $^{1,3}$MLCT and $^3$MC states. This is not the case of the latter two (7131-7135 eV and 7136-7143 eV), which are slightly non-linear. Indeed, these actually better reflect the population kinetics shown in Figure 2b. This difference derives from the varying sensitivity of the two regions. The former is most sensitive to the electronic structure, the latter the geometric structure. Indeed, as recently shown by Lemke *et al.*[23] the higher lying resonances in the XANES regions are not only sensitive to the position of the wavepacket, but also to higher moments of the wavepacket distribution, e.g. width. This is consistent with the vibrationally very hot wavepacket in the $^3$MC state.

The kinetics of each of the 4 spectral regions are imprinted, to a greater or lesser extent with the 300 fs oscillations associated with the wavepacket dynamics along $\nu_6$. This is least clear in latter two (7131-7135 eV and 7136-7143 eV), which is because of the sensitivity of the spectra features to both the position and width of the wavepacket, which somewhat convolute these transient features. These spectral changes associated with these dynamics, once a realistic photolysis yield of ~10% is included, are ~0.01% of the spectral features in the ground state and are therefore similar to those reported in ref.[22]. These are about an order of magnitude smaller than the coherent wavepacket motion reported for $[Fe(bipy)_3]^{2+}$ in ref.[23], which is consistent with the transient absorption study of ref.[11] showing only weak wavepacket oscillations.

### 3.3 X-ray Emission (XES)

Complementary to the XANES spectra presented in the previous section is XES, which provides a direct probe of the electronic structure of the occupied density of states and the spin state of the absorbing atom. The sensitivity of the latter derives from the electron exchange integrals, which is a short range interaction around the absorbing atom. This is highlighted in Figure 5 showing the K$\alpha_{1,2}$, K$\beta_{1,3}$ and K$\beta_{2,5}$ emission spectra for $[Fe(bmip)_2]^{2+}$ simulated at a distorted geometry along $\nu_6$ where the $^3$MLCT is the lowest triplet state. The red trace is the ground state spectrum of $[Fe(bmip)_2]^{2+}$, the green trace is the lowest triplet state, i.e. a $^3$MLCT and the blue trace is $[Fe(bmip)_2]^{3+}$, i.e. one electron removed from Fe, mimicking its electronic structure after excitation into an MLCT state. Adopting this approximation

assumes the inability of these emission spectra to differentiate between the $^{1,3}$MLCT. As can be seen, for both K$\alpha_{1,2}$ and K$\beta_{1,3}$ this approximation holds, as evidenced by the similarity between the blue and green traces. However, the same cannot be said for K$\beta_{2,5}$ emission. In this case, the direct probing of the occupied valence molecular orbitals provides strong sensitivity of the electronic structure of the ligands[58–60], although this comes at the cost of a significant sacrifice of cross section and therefore experimental acquisition time[22,63].

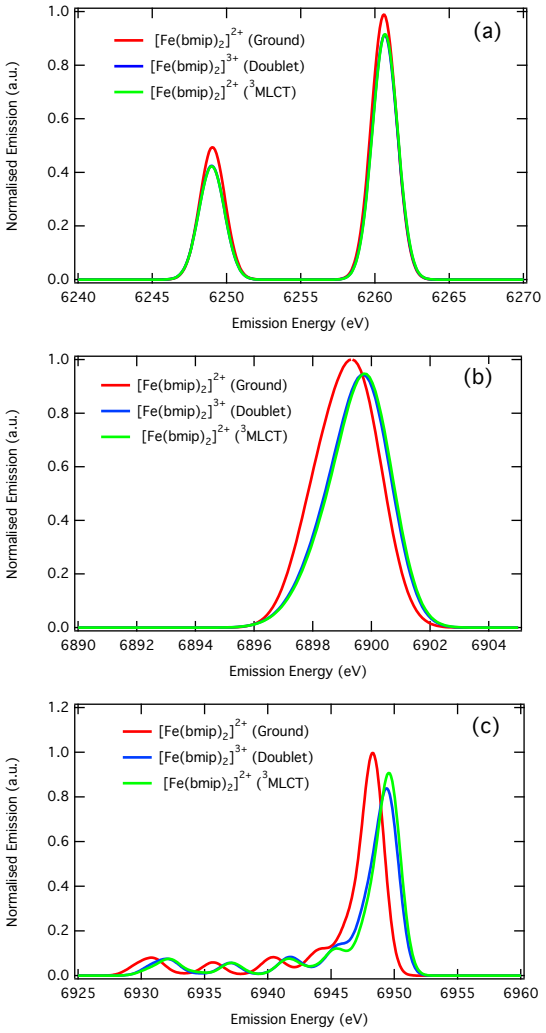


**Fig. 5** The K$\alpha$ (a), K$\beta_{1,3}$ (b) and K$\beta_{2,5}$ (c) XES spectra of $[Fe(bmip)_2]^{2+}$ at a slightly distorted geometry for which the $^3$MLCT is the lowest triplet excited state. The ground state (i.e. singlet) spectrum is shown in red, the ground state triplet (i.e. lowest $^3$MLCT) is shown in green and the spectrum for $[Fe(bmip)_2]^{3+}$, i.e. a doublet Fe(III) used to simulate MLCT excited states is shown in blue.

Figure 6a shows the ground state (black) Fe K$\beta_{1,3}$ emission spectrum of $[Fe(bmip)_2]^{2+}$ and the transient spectra (red traces) corresponding to the $^{1,3}$MLCT and $^3$MC[61]. The former are simulated using the approximation (i.e. $[Fe(bmip)_2]^{3+}$) described above, while the latter is simulated using unrestricted density functional simulations in the triplet state[61]. The transient spectra for the $^{1,3}$MLCT states are dominated by a shift of the emission energy associated with the larger nuclear charge on the Fe, in contrast the transient of $^3$MC indicates a broader emission as well as a shift to higher energies as observed for $[Fe(bipy)_3]^{2+}$[8].

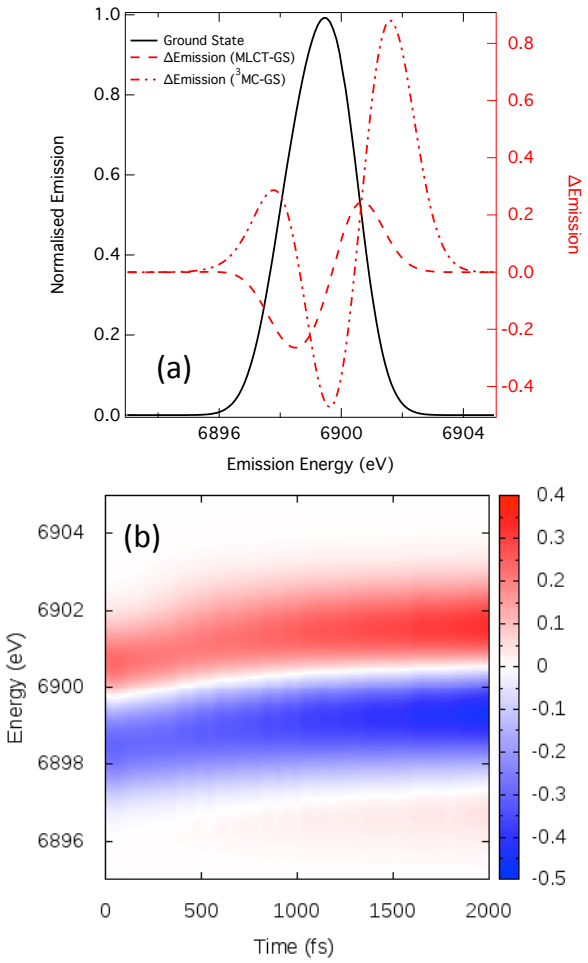


**Fig. 6** (a) The simulated ground state Fe K-edge XES spectra and transient spectra corresponding to $^{1,3}$MLCT-GS (dashed line) and $^3$MC-GS (dotted and dashed line). (b) The transient XANES spectrum as a function of time, during 2 ps after photoexitation.

Figure 6b plots the spectral evolution as a function of time. This shows an increase in the intensity of the main features associated with an increasing population of the $^3$MC states, as well as shift of the main positive and negative features to large emission energies as would be expected from Figure 6a. As reported previously in ref.[22] and expected for a core-core transition, these spectra exhibit no signature of the coherent wavepacket dynamics.

## 4 Discussion and Conclusions

Building on our recent quantum dynamics simulations studying the ultrafast photoexcited dynamics of $[Fe(bmip)_2]^{2+}$[24], in this present work we reinforce the ability of X-ray spectroscopy to reveal fine details about excited state dynamics, including coherent wavepacket motion around the absorbing atom. In addition, the spectral signatures in the XANES region for the two sets of excited states ($^{1,3}$MLCT and $^3$MC) are shown to be largely out of phase with each other. Consequently, a change in sign of the transient

signal provides a clear signature of the switching between the two manifolds. Indeed, this was recently used for $[Fe(bipy)_3]^{2+}$, albeit for a significantly shorter time[23]. We also confirm that X-ray emission, with the exception of K$\beta_{2,5}$, is not an effective approach to retrieve coherent wavepacket motion, and consequently is best suited to probing the character of the electronic structure and spin state of the absorbing atom. However, it is emphasised that the local nature of the electron exchange interaction means that the changes must be associated with those on the absorbing atom and not necessarily the molecule as a whole.

Importantly, the details of the excited state dynamics that would emerge from an experimental study on the present system suggests that in comparison to other time-resolved spectroscopies and especially in comparison to the transient optical absorption study on $[Fe(bmip)_2]^{2+}$reported in ref.[11], femtosecond X-ray spectroscopic studies are unlikely to shed significantly new insight on the photoexcited decay mechanisms. Here, one should bear in mind that the strength of X-ray spectroscopy is providing a local interpretation around the absorbing atom. Consequently, its use will be most valuable in disentangling the dynamics of complex systems which may exhibit important optically dark states and which can give a large number of broad overlapping bands, obvious examples in this direction are multi-nuclear metal complexes[15] or nanoparticles[62].

Moving forward, an increasing emphasis should be placed upon obtaining sensitivity to the electronic structure of the ligands via K$\beta_{2,5}$ XES. The biggest challenge for these experiments is the low cross section, which means that recording a transient spectrum with a reasonable signal to noise ratio will require $\sim 10^{17}$ incident photons on the sample[22,63]. This equates to $\sim 10^5$ X-FEL pulses. Such a high number of pulses will only be realistic with the development of a high-repetition X-FELs, such as the European X-FEL. Nevertheless, this would yield the most detailed insight into excited state dynamics. Importantly, as recently demonstrated by Wernet *et al.*[16], if implemented within a resonant inelastic X-ray scattering (RIXS) setup, it would open the opportunity to probe transitions corresponding to negative energy transfers. These transitions are those whose incident photon energy is smaller than the scattered photon energy, and therefore correspond exclusively to electronically excited states. The characterisation and dynamical evolution of these transitions, without a strong background arising from molecules in their ground state could provide crucial insights into excited state dynamics.

## 5 Acknowledgements

TJP acknowledges support from the Leverhulme trust grant RPG-2016-103. This work is also supported by the European Research Council via contract ERC-StG-259709 (X-cited!), the 'Lendület' (Momentum) Program of the Hungarian Academy of Sciences (LP2013-59), and the Hungarian Scientific Research Fund (OTKA) under contract K29724 and the People Programme (Marie Curie Actions) of the European Union's Seventh Framework Programme (FP7/2007-2013) under REA grant agreement number 609405 (COFUNDPostdocDTU).

## References

1 M. Chergui, *Dalton Trans.*, 2012, **41**, 13022–13029.
2 V. W.-W. Yam and K. M.-C. Wong, *Chemical Communications*, 2011, **47**, 11579–11592.
3 A. Barbieri, G. Accorsi and N. Armaroli, *Chemical Communications*, 2008, 2185–2193.
4 Z. R. Grabowski, K. Rotkiewicz and W. Rettig, *Chemical reviews*, 2003, **103**, 3899–4032.
5 M. Delor, P. A. Scattergood, I. V. Sazanovich, A. W. Parker, G. M. Greetham, A. J. Meijer, M. Towrie and J. A. Weinstein, *Science*, 2014, **346**, 1492–1495.
6 A. Hagfeldt and M. Graetzel, *Chemical Reviews*, 1995, **95**, 49–68.
7 W. J. Youngblood, S.-H. A. Lee, K. Maeda and T. E. Mallouk, *Accounts of chemical research*, 2009, **42**, 1966–1973.
8 W. Zhang, R. Alonso-Mori, U. Bergmann, C. Bressler, M. Chollet, A. Galler, W. Gawelda, R. G. Hadt, R. W. Hartsock, T. Kroll, K. S. Kjaer, K. Kubiček, H. T. Lemke, H. W. Liang, D. A. Meyer, M. M. Nielsen, C. Purser, J. S. Robinson, E. Solomon, Z. Sun, D. Sokaras, T. B. van Driel, G. Vanko, T.-C. Weng, D. Zhu and K. J. Gaffney, *Nature*, 2014, **509**, 345–348.
9 G. Auböck and M. Chergui, *Nature chemistry*, 2015, **7**, 629–633.
10 A. Hauser, *Spin Crossover in Transition Metal Compounds II*, Springer, 2004, pp. 155–198.
11 Y. Liu, T. Harlang, S. Canton, P. Chabera, K. Suarez-Alcantara, A. Fleckhaus, D. A. Vithanage, E. Göransson, A. Corani, R. Lomoth, V. Sundström and K. Wärnmark, *Chemical Communications*, 2013, **49**, 6412.
12 RM van der Veen, TJ Penfold, AH Zewail,*Structural Dynamics*, 2015, **2**, 024302.
13 C. Milne, T. Penfold and M. Chergui, *Coordination Chemistry Reviews*, 2014, **277**, 44-68.
14 C. Bostedt, S. Boutet, D. M. Fritz, Z. Huang, H. J. Lee, H. T. Lemke, A. Robert, W. F. Schlotter, J. J. Turner and G. J. Williams, *Reviews of Modern Physics*, 2016, **88**, 015007.
15 S. E. Canton, K. S. Kjær, G. Vankó, T. B. van Driel, S.-i. Adachi, A. Bordage, C. Bressler, P. Chabera, M. Christensen, A. O. Dohn *et al.*, *Nature communications*, 2015, **6**, 6359.
16 P. Wernet, K. Kunnus, I. Josefsson, I. Rajkovic, W. Quevedo, M. Beye, S. Schreck, S. Grubel, M. Scholz, D. Nordlund, W. Zhang, R. W. Hartsock, W. F. Schlotter, J. J. Turner, B. Kennedy, F. Hennies, F. M. F. de Groot, K. J. Gaffney, S. Techert, M. Odelius and A. Föhlisch, *Nature*, 2015, **520**, 78–81.
17 M. Minitti, J. Budarz, A. Kirrander, J. Robinson, D. Ratner, T. Lane, D. Zhu, J. Glownia, M. Kozina, H. Lemke *et al.*, *Physical review letters*, 2015, **114**, 255501.
18 K. H. Kim, J. G. Kim, S. Nozawa, T. Sato, K. Y. Oang, T. W. Kim, H. Ki, J. Jo, S. Park, C. Song *et al.*, *Nature*, 2015, **518**, 385–389.
19 T. Penfold, C. Milne and M. Chergui, *Advances. in Chemical Physics*, 2013, **153**, 1–41.
20 G. Capano, T. J. Penfold, U. Rothlisberger and I. Tavernelli,

*Chimia*, 2014, **68**, 227–230.
21 G. Capano, M. Chergui, U. Rothlisberger, I. Tavernelli and T. J. Penfold, *The Journal of Physical Chemistry A*, 2014, **118**, 9861-9869.
22 G. Capano, C. J. Milne, M. Chergui, U. Rothlisberger, I. Tavernelli and T. J. Penfold, *Journal Of Physics B-Atomic Molecular And Optical Physics*, 2015, **48**, 1–11.
23 H. T. Lemke, K. S. Kjær, R. Hartsock, T. B. van Driel, M. Chollet, J. Glownia, S. Song, D. Zhu, E. Pace, M. M. Nielsen *et al.*, *arXiv preprint arXiv:1511.01294*, 2016.
24 M. Pápai, T. Rozgonyi, G. Vanko and T. Penfold, *In Press J. Phys. Chem. Lett*, 2016, DOI: 10.1021/acs.jpclett.6b00711.
25 H. Köppel, W. Domcke and L. S. Cederbaum, 1984, **57**, 59–246.
26 J. Eng, C. Gourlaouen, E. Gindensperger and C. Daniel, *Accounts of chemical research*, 2015, **48**, 809–817.
27 A. D. Becke, *The Journal of Chemical Physics*, 1993, **98**, 5648–5652.
28 C. Lee, W. Yang and R. G. Parr, *Phys. Rev. B*, 1988, **37**, 785–789.
29 S. Vosko, L. Wilk and M. Nusair, *Canadian Journal of physics*, 1980, **58**, 1200–1211.
30 M. Reiher, O. Salomon and B. Artur Hess, *Theoretical Chemistry Accounts*, 2001, **107**, 48–55.
31 S. Hirata and M. Head-Gordon, *Chemical Physics Letters*, 1999, **314**, 291–299.
32 F. Neese, *Wiley Interdisciplinary Reviews-Computational Molecular Science*, 2012, **2**, 73–78.
33 F. Wang and T. Ziegler, *The Journal of Chemical Physics*, 2005, **123**, 154102.
34 C. Fonseca Guerra, J. G. Snijders, G. Te Velde and E. J. Baerends, *Theoretical Chemistry Accounts*, 1998, **99**, 391–403.
35 S. van Gisbergen, J. Snijders and E. Baerends, *Computer Physics Communications*, 1999, **118**, 119 – 138.
36 *ADF2014.07, SCM, Theoretical Chemistry, Vrije Universiteit, Amsterdam, The Netherlands*, Scientific Computation and Modelling, 2014.
37 E. v. Lenthe, E. J. Baerends and J. G. Snijders, *The Journal of Chemical Physics*, 1993, **99**, 4597–4610.
38 E. van Lenthe, E. J. Baerends and J. G. Snijders, *The Journal of Chemical Physics*, 1994, **101**, 9783–9792.
39 H.-D. Meyer, U. Manthe and L. S. Cederbaum, *Chemical Physics Letter*, 1990, **165**, 73–78.
40 M. H. Beck, A. Jäckle, G. A. Worth and H.-D. Meyer, *Phys. Rep.*, 2000, **324**, 1–105.
41 Y. Joly, *Physical Review B*, 2001, **63**, 125120.
42 S. A. Guda, A. A. Guda, M. A. Soldatov, K. A. Lomachenko, A. L. Bugaev, C. Lamberti, W. Gawelda, C. Bressler, G. Smolentsev, A. V. Soldatov and Y. Joly, *Journal Of Chemical Theory And Computation*, 2015, **11** 4512–4521.
43 O. Bunău and Y. Joly, *Journal of Physics-Condensed Matter*, 2009, **21**, 345501.
44 M. A. Beckwith, M. Roemelt, M.-N. Collomb, C. DuBoc, T.-C. Weng, U. Bergmann, P. Glatzel, F. Neese and S. DeBeer, *Inorganic chemistry*, 2011, **50**, 8397–8409.
45 N. Lee, T. Petrenko, U. Bergmann, F. Neese and S. DeBeer, *Journal of the American Chemical Society*, 2010, **132**, 9715–9727.
46 A. Schäfer, H. Horn and R. Ahlrichs, *The Journal of Chemical Physics*, 1992, **97**, 2571–2577.
47 F. Weigend and R. Ahlrichs, *Physical Chemistry Chemical Physics*, 2005, **7**, 3297–3305.
48 B. A. Hess, C. M. Marian, U. Wahlgren and O. Gropen, *Chemical Physics Letters*, 1996, **251**, 365–371.
49 M. Stener, *Chemical Physics Letters*, 2003, **373**, 115–123.
50 N. Besley, M. Peach and D. Tozer, *Physical Chemistry Chemical Physics*, 2009, **11**, 10350.
51 S. DeBeer-George, T. Petrenko and F. Neese, *Journal Of Physical Chemistry A*, 2008, **112**, 12936–12943.
52 G. Capano, T. J. Penfold, N. A. Besley, C. J. Milne, M. Reinhard, H. Rittmann-Frank, P. Glatzel, R. Abela, U. Rothlisberger, M. Chergui and I. Tavernelli, *Chemical Physics Letters*, 2013, **580**, 179–184.
53 G. Bunker, *Introduction to XAFS*, Cambridge University Press, 2010.
54 F. de Groot, *Chemical Reviews*, 2001, **101**, 1779–1808.
55 V. Briois, P. Sainctavit, G. Long and F. Grandjean, *Inorganic Chemistry*, 2001, **40**, 912–918.
56 T. J. Penfold, S. Karlsson, G. Capano, F. A. Lima, J. Rittmann, M. Reinhard, M. H. Rittmann-Frank, O. Braem, E. Baranoff, R. Abela, I. Tavernelli, U. Rothlisberger, C. J. Milne and M. Chergui, *The Journal of Physical Chemistry A*, 2013, **117**, 4591–4601.
57 W. Gawelda, V. Pham, M. Benfatto, Y. Zaushitsyn, M. Kaiser, D. Grolimund, S. Johnson, R. Abela, A. Hauser, C. Bressler and M. Chergui, *Physical Review Letters*, 2007, **98**, 057401.
58 C. J. Pollock and S. DeBeer, *Accounts of Chemical Research*, 2015, **48**, 2967–2975.
59 G. Vankó, T. Neisius, G. Molnár, F. Renz, S. Kárpáti, A Shukla, F. M. F. de Groot *The Journal of Physical Chemistry B*, 2006, **110**, 11647–1165**48**, 2967–2975.
60 G. Vankó, A. Bordage, P. Glatzel, E. Gallo, M. Rovezzi, W. Gawelda, A. Galler, C. Bressler, G. Doumy, AM. March, EP Kanter, L. Young, SH Southworth, SE Canton, J. Uhlig, G. Smolentsev, V Sundstrom, K Haldrup, TB van Driel, MM Nielsen, KS Kjaer, HT Lemk *Journal of Electron Spectroscopy and Related Phenomena*, 2013, **188**, 166–171.
61 It is noted that at distorted geometries along mode 6, the lowest triplet state is no longer the metal centred state, as exploited in Figure 5. This means an uDFT simulation for the metal centred state is strictly no longer valid. However, the fraction of wavepacket that visits this region of the potential is very small and therefore this has no influence on the transient spectra reported.
62 M. Rittmann-Frank, C. Milne, J. Rittmann, M. Reinhard, T. Penfold and M. Chergui, *Angewandte Chemie Int. Ed.*, 2013, **53**, 5858-5862.
63 A. M. March, T. A. Assefa, C. Bressler, G. Doumy, A. Galler,

W. Gawelda, E. P. Kanter, Z. Németh, M. Pápai, S. H. Southworth *et al.*, *The Journal of Physical Chemistry C*, 2015, **119**,14571-14578.